



Article

Climate Prediction of Satellite-Based Spring Eurasian Vegetation Index (NDVI) using Coupled Singular Value Decomposition (SVD) Patterns

Liuqing Ji 1,2 and Ke Fan 1,2,*

- Nansen-Zhu International Research Centre, Institute of Atmospheric Physics, Chinese Academy of Sciences, Beijing 100029, China; jiliuqing@mail.iap.ac.cn
- ² University of Chinese Academy of Sciences, Beijing 100049, China
- * Correspondence: fanke@mail.iap.ac.cn; Tel.: +86-010-8299-5322

Received: 9 July 2019; Accepted: 10 September 2019; Published: 12 September 2019



Abstract: Satellite-based normalized difference vegetation index (NDVI) data are widely used for estimating vegetation greenness. Seasonal climate predictions of spring (April-May-June) NDVI over Eurasia are explored by applying the year-to-year increment approach. The prediction models were developed based on the coupled modes of singular value decomposition (SVD) analyses between Eurasian NDVI and climate factors. One synchronous predictor, the spring surface air temperature from the NCEP's Climate Forecast System (SAT-CFS), and three previous-season predictors (winter (December–January–February) sea-ice cover over the Barents Sea (SICBS), winter sea surface temperature over the equatorial Pacific (SSTP), and winter North Atlantic Oscillation (NAO) were chosen to develop four single-predictor schemes: the SAT-CFS scheme, SICBS scheme, SSTP scheme, and NAO scheme. Meanwhile, a statistical scheme that involves the three previous-season predictors (i.e., SICBS, SSTP, and NAO) and a hybrid scheme that includes all four predictors are also proposed. To evaluate the prediction skills of the schemes, one-year-out cross-validation and independent hindcast results are analyzed, revealing the hybrid scheme as having the best prediction skill. The results indicate that the temporal correlation coefficients at 92% of grid points over Eurasia are significant at the 5% significance level in the hybrid scheme, which is the best among all the schemes. Furthermore, spatial correlation coefficients (SCCs) of the six schemes are significant at the 1% significance level in most years during 1983–2015, with the averaged SCC of the hybrid scheme being the highest (0.60). The grid-averaged root-mean-square-error of the hybrid scheme is 0.04. By comparing the satellite-based NDVI value with the independent hindcast results during 2010–2015, it can be concluded that the hybrid scheme shows high prediction skill in terms of both the spatial pattern and the temporal variability of spring Eurasian NDVI.

Keywords: Eurasia; spring NDVI; winter sea-ice cover; Barents Sea; ENSO; winter NAO; year-to-year increment; climate prediction; hybrid dynamical–statistical model

1. Introduction

Unequivocal global warming since the mid-19th century has been revealed. In the Northern Hemisphere, the last three decades were the warmest of the last 1400 years [1]. The increased surface air temperature could prompt a longer growing season, increased photosynthetic activity and respiration, and an increase in productivity of terrestrial vegetation [2–7]. Meanwhile, terrestrial vegetation interacts with the climate through the surface albedo, hydrological processes, roughness, carbon exchange, and so on [8–14]. In Eurasia, the rising temperature has led to the northward extension of the forest treeline into tundra areas [15,16]. The changes in Eurasian vegetation not only have important effects on regional climate, such as the East Asian atmospheric circulation, Eurasian temperature and

moisture etc., but also have effects on global temperatures and the carbon cycle [17–22]. The vegetation biomass over Eurasia experiences its most notable increases during spring (April–May–June), and the spring vegetation biomass has a considerable bearing on the total vegetation biomass of the year [23–25]. As such, seasonal climate predictions of spring vegetation over Eurasia are beneficial for the understanding of local and large-scale short-term climatic changes.

Satellite-based remote-sensing data are widely used for estimating crop yields, vegetation greenness, and even precipitation in some arid regions [26–33]. They are especially helpful in regions where field observations are sparse. Among them, the normalized difference vegetation index (NDVI) is a proxy of vegetation vigor obtained from satellite data of the red and near-infrared reflectance, which is widely used as an indicator of vegetation greenness under many conditions [34–39]. The accurate seasonal prediction of NDVI is important for our understanding of short-term climatic changes and agricultural policymaking. There are a few studies focused on the climate prediction of NDVI [40–44], with most having chosen predictors of local climate factors, such as temperature, soil moisture, and precipitation. However, large-scale climate conditions might be better predictors because their patterns provide a conceptual framework and a broader understanding of observed changes in the local physical environment [45–47]. Meanwhile, with the development of new statistical prediction methods, models can be improved in terms of predicting both the spatial pattern and the temporal variability of NDVI. Therefore, this study aims to develop more effective prediction models for NDVI based on large-scale climate factors through the application of new prediction methods.

It is widely recognized that the local spring surface air temperature plays a key role in the growth of spring Eurasian vegetation [4,48–50]. However, these synchronous observed surface air temperature data are of course not available before spring. Therefore, this study employed spring surface air temperature data from a state-of-the-art coupled dynamic prediction system (version 2 of the National Centers for Environmental Prediction's Climate Forecast System (CFSv2)) as a synchronous predictor in the prediction model. Aside from the current-season predictor, previous-season climatic factors are also known to be influential for spring Eurasian NDVI, especially large-scale climate patterns, such as El Niño, the winter North Atlantic Oscillation (NAO), winter Arctic polar vortex, winter Arctic sea-ice cover, and winter snow cover [23,51–54]. These relationships between spring Eurasian NDVI and climate factors broaden the physical basis for the seasonal prediction of spring Eurasian vegetation. Considering both the current-season and previous-season predictors, a hybrid dynamical–statistical model was developed. This hybrid prediction approach has been used previously in the seasonal prediction of East Asian summer monsoon [55], summer precipitation [56], and spring dust weather frequency [57], and has been proven to be an effective method.

A singular value decomposition (SVD) analysis was used to obtain pairs of spatial patterns between two variables that are optimally correlated [58]. The correlated SVD spatial patterns of the predictand and the predictors have been used to develop statistical prediction models for East Asian precipitation [56,59] and winter temperature [60], amongst others, demonstrating good prediction skill in terms of the spatiotemporal variability patterns of the predictand. Therefore, a prediction approach based on coupled spatiotemporal variability patterns via SVD analysis to establish prediction models was used. Meanwhile, the year-to-year increment approach proposed by Fan et al. [61] has been employed in previous studies to improve seasonal climate prediction skills [55,57,62]. The year-to-year increment of a variable means the difference in the variable between the current year and the previous year (difference in years; hereafter DY for short) [61]. In the prediction process, the DY is predicted first, and added to the observed variable V, for example, in the previous year to obtain the predicted variable V in the current year (that is: predicted V (current year) = predicted DY + V (previous year)). The amplitude of the DY of a variable is approximately twice the amplitude of the variable itself or its anomaly with respect to its multi-year average [63]. Therefore, the signal for both the predictand and the predictors can be amplified, and the prediction skill can be improved. The year-to-year increment approach has already proved successful in improving seasonal climate predictions of East Asian summer monsoon rainfall [55,61], winter monsoon [62], typhoon frequency [64,65], and so on. Therefore, the year-to-year increment approach was applied with confidence in the present study.

Remote Sens. 2019, 11, 2123 3 of 21

This study aims to develop prediction models for spring Eurasian NDVI based on current-season and previous-season climate factors. The models are expected to predict spring (April–May–June-averaged) NDVI over Eurasia (50°–65°N, 50°–120°E) in February. A new prediction method based on SVD paired modes of the predictand and the predictors was applied, which is expected to improve the prediction skill of spring Eurasian NDVI. The rest of this paper is organized as follows. In Section 2, the materials and methods used in this study are introduced. The predictors and their physical linkages to Eurasian NDVI are illustrated in Section 3. Section 4 reports the verification results of the prediction models. Finally, a conclusion is given in Section 5.

2. Materials and Methods

2.1. NDVI and Climate Data

The NDVI data used in this study were from the third-generation NDVI dataset (NDVI3g) derived from the advanced very high-resolution radiometer instruments onboard the National Oceanic and Atmospheric Administration (NOAA) series of meteorological satellites [37,66]. As chlorophyll absorbs red light and the mesophyll leaf structure scatters near-infrared light, the vegetation greenness, or vigor, can be represented by the combination of the earth surface reflectance of radiation at red and near-infrared wavelengths [67–69]. The NDVI was calculated based on the red spectral band (0.58–0.68 μ m) and the near-infrared spectral band (0.725–1.10 μ m) reflectance [NDVI = (NIR – RED)/(NIR + RED)]. The NDVI values of vegetation regions are greater than 0.1 [70,71]. The original global AVHRR data of the Global Area Coverage format at 4 km spatial and daily temporal resolution were processed (including sampling, calibration, noise removal, mapping, gap treatment, etc.) by the Global Inventory Modeling and Mapping Studies (GIMMS) archiving from 1981 through to the present day [72]. GIMMS produces the NDVI3g dataset at a 1/12° × 1/12° spatial resolution and 1/24 a year temporal resolution. Then, the NDVI3g dataset was reprojected into a monthly dataset at a 1.0° × 1.0° spatial resolution to suppress data noise.

The first spatial mode of the empirical orthogonal function (EOF) of Eurasian NDVI shows large values of approximately $(50^{\circ}-65^{\circ}\text{N}, 50^{\circ}-120^{\circ}\text{E})$ (Figure 1a), which means significant variations of NDVI. The time series of the first mode of EOF shows the characteristic of interannual variability (Figure 1b). Therefore, our prediction of Eurasian NDVI (NDVIEA) was focused on the region of $(50^{\circ}-65^{\circ}\text{N}, 50^{\circ}-120^{\circ}\text{E})$. Figure 1c indicates that Eurasian NDVI experiences a rapid increase from April to June. Considering the importance of spring vegetation to the climate system, the focus is on the prediction of spring NDVIEA.

Monthly climate data were derived from the European Centre for Medium-Range Weather Forecast's interim reanalysis dataset (ERA-Interim) at the $0.75^{\circ} \times 0.75^{\circ}$ spatial resolution during 1982–2015 [73], including the variables of monthly sea level pressure, zonal and meridional wind, geopotential height, 2 m air temperature, and soil temperature (level 1; 0.07 m). The monthly sea-ice cover and sea surface temperature data from the Met Office Hadley Centre observational datasets at the $1.0^{\circ} \times 1.0^{\circ}$ spatial resolution during 1982–2015 were also used [74]. The satellite-derived monthly snow water equivalent data derived from the National Snow and Ice Data Center are available at 25 km Equal-Area Scalable Earth Grids from 1982 to 2007 [75]. The monthly snow cover data in the 89×89 cells Northern Hemisphere grid during 1982–2015 were derived from the Rutgers University Global Snow Lab and transformed to a $2.5^{\circ} \times 2.5^{\circ}$ spatial resolution in this study [76]. The monthly NAO index and Niño3 index during 1982–2015 were derived from the publicly available NOAA-CPC database [77,78].

The spring monthly surface air temperature at a $1.0^{\circ} \times 1.0^{\circ}$ spatial resolution during 1982–2015 were derived from CFSv2 [79]. CFSv2 makes retrospective forecasts using initial states from the Climate Forecast System Reanalysis from 1982 to 2010 and onward to calibrate subsequent operational real-time predictions. The nine-month forecast surface air temperature data initialized in March during 1982–2015 of April to June was used in this study.

Remote Sens. 2019, 11, 2123 4 of 21

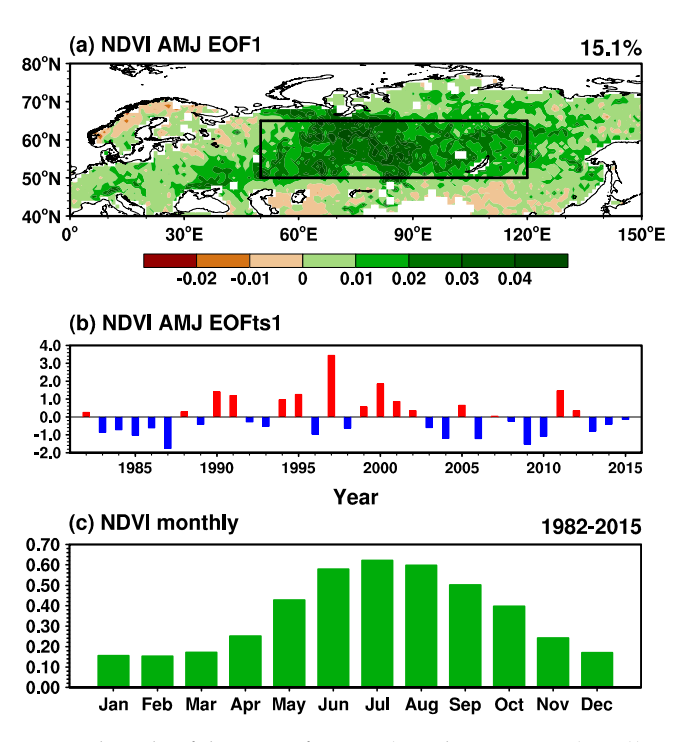


Figure 1. (a) The first spatial mode of the EOF of spring (April–May–June (AMJ)) normalized difference vegetation index (NDVI) during 1982–2015. The variance explained by the EOF mode is shown above the top right-hand corner. (b) Corresponding time series of the first EOF mode. (c) Monthly area-averaged NDVI over $(40^{\circ}-80^{\circ}\text{N}, 0^{\circ}-150^{\circ}\text{E})$ during 1982–2015.

2.2. Methods

The year-to-year increment approach was applied in the prediction and analysis processes:

$$V_{DY}(t) = V(t) - V(t-1),$$
 (1)

where V(t) is a variable in the current year; V(t-1) is the variable one year before V(t); and $V_{DY}(t)$ is the DY of the variable. On the one hand, the DY can amplify the interannual signal for both the predictand and the predictors compared to the anomalies of variables. On the other hand, the prediction based on the year-to-year increment approach can obtain the interdecadal variability of variables by employing V(t-1) [61]. Therefore, the year-to-year increment approach was applied to achieve higher prediction skill.

The prediction approach based on the coupled spatiotemporal variability patterns was used. Firstly, SVD analyses are used to extract the pairs of spatial patterns of the predictand and predictor that are optimally correlated [58]:

$$X(t,x) = \sum_{i=1}^{m} U_i(x)A_i(t),$$
 (2)

$$Y(t,x) = \sum_{i=1}^{m} R_i(x)B_i(t),$$
(3)

In the formulae, X(t,x) and Y(t,x) are the DYs of the predictor and predictand, respectively; m represents the number of all the SVD modes; $U_i(x)$ and $R_i(x)$ represent the singular vector of the ith mode of the predictor and predictand, respectively; $A_i(t)$ and $B_i(t)$ indicate the corresponding time expansion coefficients of the ith mode. Then, the predicted time expansion coefficients for each SVD mode of the predictand $\widetilde{B}_i(t)$ are obtained using linear regression of $A_i(t)$ of the predictor:

$$\widetilde{B}_i(t) = \beta_i A_i(t) + \varepsilon_i, \ i = 1, \dots, m,$$
 (4)

Remote Sens. **2019**, 11, 2123 5 of 21

Here, β_i is the linear regression coefficient of the ith mode, and ε_i is the residual. Then, the predictand can be obtained by the predicted time expansion coefficients $\widetilde{B}_i(t)$ and the singular vector:

$$\widetilde{Y}_k(t,x) = \sum_{i=1}^m R_i(x)\widetilde{B}_i(t), \tag{5}$$

in which $\widetilde{Y}_k(t,x)$ is the DY of the predicted variable based on the kth single predictor. In this study, more than one predictor was used in the statistical and hybrid models. The predictors are weighted using the multiple linear regression method:

$$\widetilde{Y}_{DY}(t,x) = b(t,x) + \sum_{k=1}^{K} a_k(t,x)\widetilde{Y}_k(t,x),$$
(6)

where $\widetilde{Y}_{DY}(t,x)$ is the DY of the predicted variable based on multiple-predictor schemes; K is the total number of predictors; $a_k(t,x)$ is the multiple linear regression coefficients. The prediction process is based on a grid-to-grid scale, which means every grid carries a different weighting. Finally, the DY of the predicted variable is added to the observed variable in the previous year to obtain the predicted variable Y in the current year:

$$\widetilde{Y}(t,x) = Y_{Obs}(t-1,x) + \widetilde{Y}_{DY}(t,x), \tag{7}$$

in which $Y_{Obs}(t-1,x)$ is the observed variable in the previous year and $\widetilde{Y}(t,x)$ is the final predicted variable in the current year.

To verify the prediction skill of the models, the one-year-out cross-validation method was used for the period 1982–2015 [80]. One year in the time span of the predictand was deleted, and the remaining years were used as the training period to develop the prediction model. The cross-validation was performed 34 times during 1982–2015, and the results were compared to the NDVI3g data to estimate the prediction skill. Meanwhile, an independent hindcast for the period 2010–2015 was also performed. The independent hindcast scheme was developed based on the previous years for the NDVI in the following year (i.e., the prediction in 2010 was based on the training period of 1982–2009; the prediction in 2015 was based on the training period of 1982–2014). This procedure was repeated six times.

The temporal and spatial correlation coefficients (TCCs and SCCs, respectively) between the cross-validated results and reanalysis data were calculated to evaluate the prediction skills. Furthermore, the root-mean-square-errors (RMSEs) are calculated:

RMSE =
$$\sqrt{\frac{\sum_{i=1}^{N} (y_i - y_{oi})^2}{N}}$$
, (8)

in which N is the number of years during the study period; y_i and y_{oi} represent the NDVI3g data and the prediction schemes' outputs, respectively.

In the verification of the physical linkages between spring NDVIEA and climate factors, composite analyses were explored based on the criterion that the normalized DY of the indexes (including sea-ice index, Ni \tilde{n} 03 index and NAO index) were greater than 0.5 or less than -0.5. Note that all the composite analysis results were based on the variables in year-to-year-increment form. The linear correlations used in this study were in the form of Pearson correlation. Furthermore, the wave activity flux for diagnosing the propagation of Rossby waves was calculated using the following formula [81]:

$$W = \frac{p \cos \phi}{2|\mathbf{U}|} \begin{pmatrix} \frac{U}{a^{2} \cos^{2} \phi} \left[\left(\frac{\partial \psi'}{\partial \lambda} \right)^{2} - \psi' \frac{\partial^{2} \psi'}{\partial \lambda^{2}} \right] + \frac{V}{a^{2} \cos \phi} \left[\frac{\partial \psi'}{\partial \lambda} \frac{\partial \psi'}{\partial \phi} - \psi' \frac{\partial^{2} \psi'}{\partial \lambda \partial \phi} \right] \\ \frac{U}{a^{2} \cos \phi} \left[\frac{\partial \psi'}{\partial \lambda} \frac{\partial \psi'}{\partial \phi} - \psi' \frac{\partial^{2} \psi'}{\partial \lambda \partial \phi} \right] + \frac{V}{a^{2}} \left[\left(\frac{\partial \psi'}{\partial \phi} \right)^{2} - \psi' \frac{\partial^{2} \psi'}{\partial \phi^{2}} \right] \\ \frac{f_{0}^{2}}{N^{2}} \left\{ \frac{U}{a \cos \phi} \left[\frac{\partial \psi'}{\partial \lambda} \frac{\partial \psi'}{\partial z} - \psi' \frac{\partial^{2} \psi'}{\partial \lambda \partial z} \right] + \frac{V}{a} \left[\frac{\partial \psi'}{\partial \phi} \frac{\partial \psi'}{\partial z} - \psi' \frac{\partial^{2} \psi'}{\partial \phi \partial z} \right] \right\} \end{pmatrix} + C_{U}M, \tag{9}$$

Remote Sens. **2019**, 11, 2123 6 of 21

in which p = (pressure/1000hPa) and $z = -H \ln p$ (H is a constant scale height); ϕ and λ are the latitude and longitude; $\mathbf{U} = (U, V, 0)^T$ represents the basic flow; a is Earth's radius; ψ represents the geostrophic streamfunction; N^2 is the buoyancy frequency squared; C_U is a vector that indicates the phase propagation in the zonal direction; and M is the wave-activity pseudomomentum.

3. Results

In this section, the chosen predictors and the reasons for choosing them are introduced. The physical mechanisms of the relationships between spring Eurasian NDVI and the predictors are explained. Then, the prediction models applying the coupled SVD patterns based on the year-to-year increment method were developed for the spring Eurasian NDVI. The one-year-out cross-validation and independent hindcasts were performed to determine and compare the accuracy of the models.

3.1. Predictors

To develop an effective prediction model, the predictors should be physically significant and statistically significantly correlated with the predictand. Based on investigation and analyses of climate factors related to NDVIEA, one current-season predictor (spring surface air temperature) and three previous-season predictors (winter sea-ice cover, sea surface temperature, and NAO) were taken into consideration.

3.1.1. Spring Surface Air Temperature over Eurasia from CFSv2

Classical statistical seasonal climate prediction is based on the premise that the physical linkages between the predictand and the previous-season predictors remain stable in the coming prediction period. However, current-season climate factors may also closely relate to the predictand. If current-season climate factors available in a dynamic climate prediction system (e.g., CFSv2) can be used as synchronous predictors, the prediction skill could be improved. A prediction model that combines previous-season and current-season predictors is called a hybrid dynamical–statistical model. This a hybrid prediction approach has been used previously in the prediction of East Asian summer monsoon [55], winter temperature [60], spring dust weather frequency [57], and so on. Considering the good performance of the hybrid approach in seasonal climate prediction, this study attempted to include current-season predictors derived from CFSv2 in the prediction schemes.

Previous studies have found that spring NDVIEA is mainly associated with the condition of spring temperature and precipitation [49,82]. The growing season of Eurasian vegetation starts in March or April. The higher spring temperature is associated with an earlier and longer growing season [2,50,83]. Previous studies have also indicated that vegetation is more related to temperature than precipitation in northern middle and high latitudes [48,84]. Thus, this study attempted to use the spring surface air temperature as a predictor. As observational or reanalysis climate data for spring were unavailable in advance, CFSv2's real-time prediction results of spring surface air temperature data were used.

Figure 2 shows the first paired mode of the SVD analysis of the DY of spring surface air temperature and NDVIEA. Note that the spring surface air temperature was derived from CFSv2 data initialized in March (over (40°–70°N, 30°–130°E), abbreviated as SAT-CFS). The SAT-CFS field shows positive anomalies and the NDVIEA field shows positive anomalies over most of Eurasia, except for a negative center near (55°–65°N, 70°–110°E) (Figure 2a,b). The first paired mode explains 58.3% of the total variance, and the correlation coefficient between the time series of expansion coefficients is 0.65 (significant at the 1% significance level; Figure 2c). Meanwhile, the prediction skill of CFSv2 was tested (Figure 3). The NDVIEA shows significant positive correlations with the Eurasian surface air temperature from ERA-Interim (Figure 3a). Furthermore, the correlation coefficients between the surface air temperature of CFSv2 and ERA-Interim are significant over most parts of Eurasia (Figure 3b). SAT-CFS not only describes important physical linkages to NDVIEA, but is also statistically significantly correlated with NDVIEA. Meanwhile, CFSv2 shows good real-time prediction skill for Eurasian spring surface air temperature. Therefore, SAT-CFS was considered as a predictor.

Remote Sens. 2019, 11, 2123 7 of 21

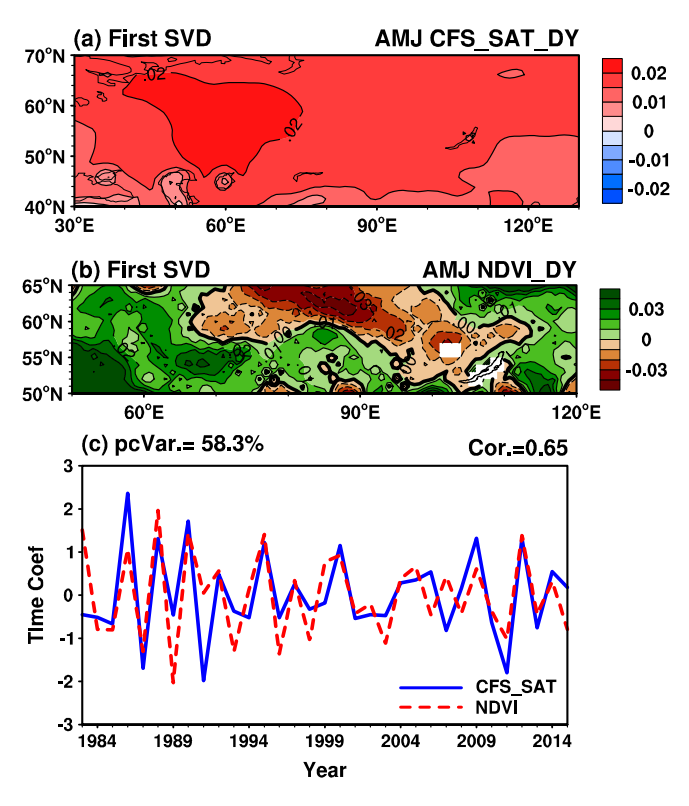


Figure 2. Spatial patterns for the first paired mode of the difference in years (DY) of (a) spring (April–May–June (AMJ)) surface air temperature (SAT) from CFSv2 and (b) spring Eurasian NDVI (NDVIEA) via a singular value decomposition (SVD) analysis during 1983–2015. (c) The corresponding normalized time series of the expansion coefficients for the paired mode; their correlation coefficient is shown above the top right-hand corner, and the variance explained by the first mode is shown above the top left-hand corner.

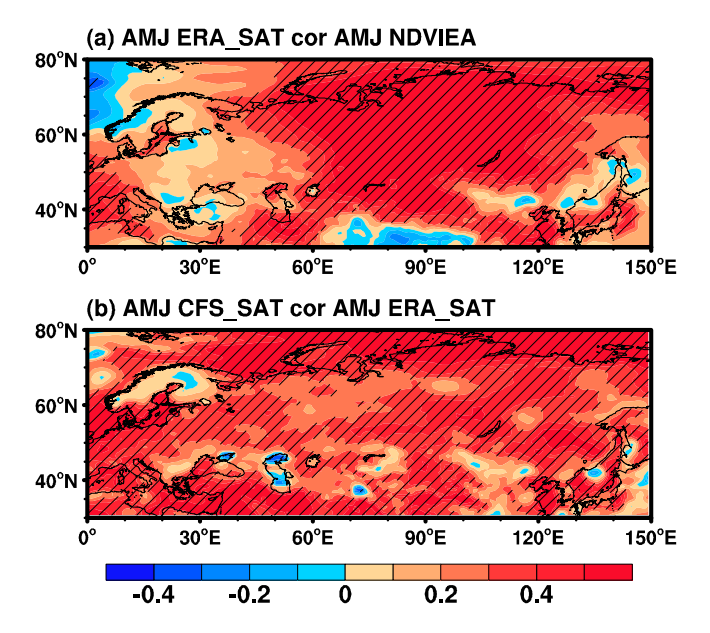


Figure 3. (a) Correlation between area-averaged spring (April–May–June (AMJ)) NDVIEA index and the surface air temperature (SAT) from ERA-Interim during 1982–2015. (b) Correlation between the spring SAT from ERA-Interim and CFSv2 during 1982–2015. Regions marked by slashes are significant ($\alpha = 0.10$; *t*-test).

Remote Sens. 2019, 11, 2123 8 of 21

3.1.2. Winter Sea-Ice Cover over the Barents Sea

The decrease in the Arctic sea-ice cover and its effects on weather and climate, especially over middle and high latitudes in the Northern Hemisphere, has become a hot topic [85–88]. Ji and Fan [53] found that the Arctic sea-ice cover is positively correlated with NDVIEA. Figure 4 depicts the leading paired mode of the SVD analysis of the DY of winter sea-ice cover over the Barents Sea, $(78^{\circ}-85^{\circ}N, 25^{\circ}-130^{\circ}E)$, abbreviated as SICBS), and spring NDVIEA. The leading SVD mode shows that the positive SICBS anomalies and the overall positive NDVIEA anomalies are optimally correlated. The leading paired mode explains 63.3% of the total variance, and the correlation coefficient between the time series of expansion coefficients is 0.67 (significant at the 1% significance level; Figure 4c).

The possible mechanism underlying the linkage between SICBS and NDVIEA has been explored by Ji and Fan [53]. An increase in SICBS might induce a Rossby wave via anomalous adiabatic heating. This anomalous Rossby wave can propagate southeastward and southward, exciting anticyclonic circulation anomalies over Eurasia. Meanwhile, anomalous westerly winds bring warm and moist air from the Atlantic to Eurasia, helping to increase the winter surface air temperature south of 70°N [53]. Therefore, the corresponding snow cover is less over Eurasia. These negative snow cover anomalies can persist from winter to spring to influence spring climate conditions that are relevant to NDVIEA. As less snow cover corresponds to a lower snow albedo, the earth surface could be heated owing to the receipt of more solar radiation. Meanwhile, less snow cover and less snowmelt might also influence surface temperatures via a reduction in latent heat [89–91]. Corresponding to an increase in winter SICBS, the spring soil temperature over Eurasia shows positive anomalies, which is favorable for higher spring NDVIEA. Therefore, Eurasian snow cover acts as a bridge between winter SICBS and spring NDVIEA, with increased winter SICBS potentially inducing increased spring NDVIEA via its positive effect on spring Eurasian soil temperatures. Thus, winter SICBS was used as a predictor of spring NDVIEA.

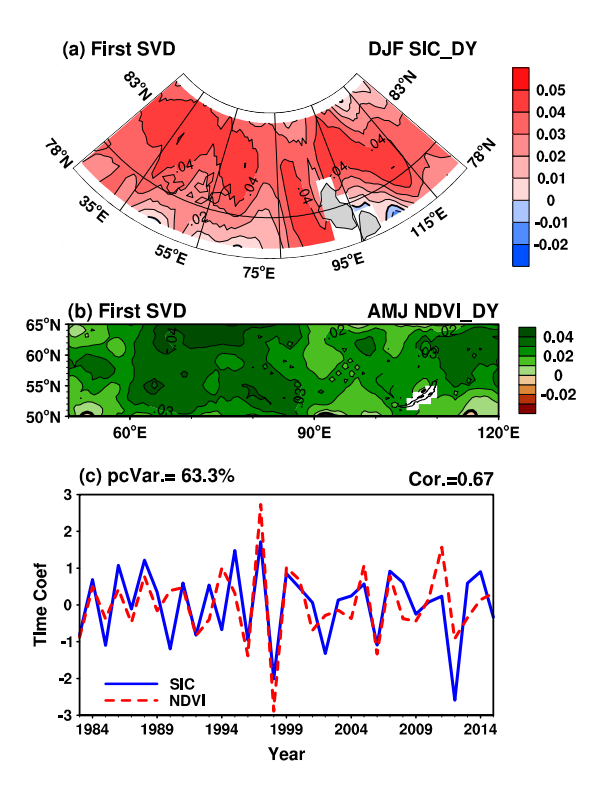


Figure 4. Spatial patterns for the first paired mode of the DY of (a) winter (December–January–February (DJF)) sea-ice cover over the Barents Sea (SICBS) and (b) spring (April–May–June (AMJ)) NDVIEA via SVD analysis during 1983–2015. (c) The corresponding normalized time series of the expansion coefficients for the paired mode; their correlation coefficient is shown above the top right-hand corner, and the variance explained by the first mode is shown above the top left-hand corner.

Remote Sens. 2019, 11, 2123 9 of 21

3.1.3. Winter El Niño

El Niño is an important aspect of the climate system that can induce changes not only in tropical weather and climate, but also subtropical and high-latitude climate via atmospheric teleconnection [92–95]. According to Li et al. [96], spring vegetation greenness over Eurasia is closely linked to El Niño events. Figure 5 depicts the first paired mode of the SVD analysis of the sea surface temperature over the equatorial Pacific and NDVIEA. The leading SVD mode of sea surface temperature shows an El Niño–like pattern, with positive sea surface temperature anomalies over the eastern equatorial Pacific. Meanwhile, as shown in Figure 5b, negative spring NDVI anomalies east of 60°E are associated with El Niño events. The variance explained by the first paired mode is 76.1%, and the correlation coefficient between their time series of expansion coefficients is 0.68 (significant at the 1% significance level). Therefore, El Niño events may have negative influences on spring NDVIEA.

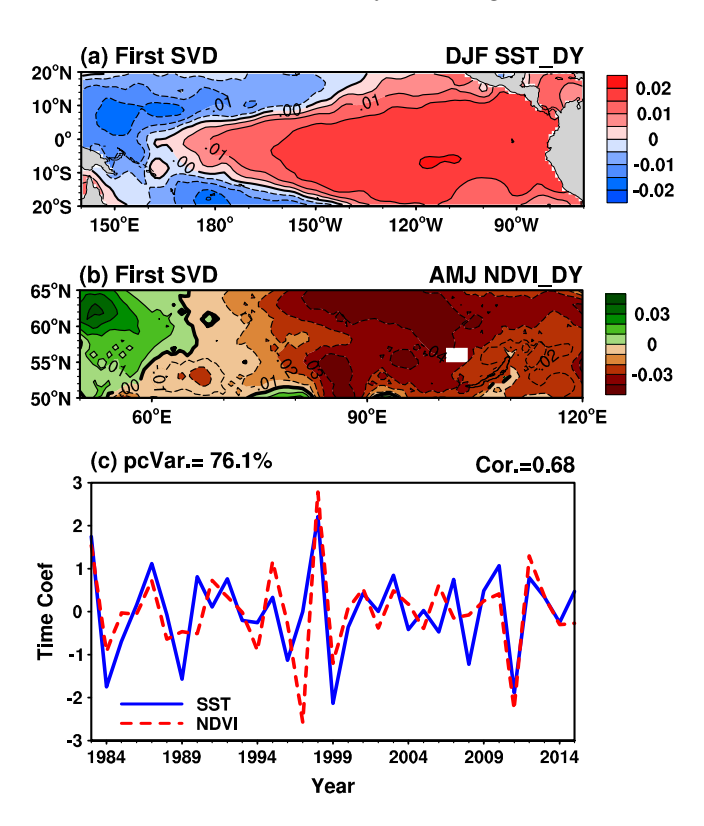


Figure 5. Spatial patterns for the first paired mode of the DY of (a) winter (December–January–February (DJF)) sea surface temperature (SST, tropical Pacific) and (b) spring (April–May–June (AMJ)) NDVIEA via SVD analysis during 1983–2015. (c) The corresponding normalized time series of the expansion coefficients for the paired mode; their correlation coefficient is shown above the top right-hand corner, and the variance explained by the first mode is shown above the top left-hand corner.

The mechanism responsible for this linkage was investigated by Li et al. [96]. The mature phase of El Niño is in winter, when the eastern Pacific shows positive sea surface temperature anomalies and the western Pacific negative anomalies. In the following spring, much of the tropical Indian Ocean warms up according to the Indian Ocean capacitor effect proposed by Xie et al. [97]. Therefore, the anomalous easterly wind that blows from the cold waters of the western Pacific to the relatively warmer waters of the North Indian Ocean strengthens in spring [98]. In turn, the sea surface temperature over the North Indian Ocean cools in spring, and this cooling persists because of positive wind–evaporation–sea surface temperature feedback [99]. The anomalously suppressed convection that results from the cooling sea surface temperature over the North Indian Ocean excites Rossby waves and can affect the Asian climate [96]. Rossby waves originating from the Bay of Bengal propagate northeastward to the Kamchatka peninsula via southern China and Japan, which excites anomalous cyclonic circulation over

a large region east to 80° E [96]. This, in turn, affects spring NDVIEA via anomalous low surface air temperatures associated with the northeasterly and northwesterly winds in the west of the anomalous cyclonic circulation centered near the Kamchatka peninsula. As El Niño events indeed have negative influences on spring NDVIEA, the winter equatorial Pacific sea surface temperature (over $(20^{\circ}\text{S}-20^{\circ}\text{N}, 140\text{E}^{\circ}-70^{\circ}\text{W})$, abbreviated as SSTP) was considered as a predictor.

3.1.4. Winter NAO

The NAO is a prominent atmospheric circulation pattern characterized by a large-scale seesaw pattern of sea level pressure between the Icelandic low and Azores high that dictates the climate variability of North America and Eurasia [100]. Li et al. [23] explored the linkage between late winter (January–February–March) NAO and spring Eurasia NDVI and found that positive-phase late winter NAO can lead to higher than average NDVIEA. In the first paired mode of the SVD analysis of sea level pressure (20°–80°N, 90°W–40°E) and NDVIEA, the sea level pressure shows a similar pattern to positive-phase NAO, and NDVIEA shows overall positive anomalies (Figure 6). The variance explained by the first paired mode is 62.5%, and the correlation coefficient between their time series of expansion coefficients is 0.58 (significant at the 1% significance level). The NAO might therefore be an important factor of influence on NDVIEA.

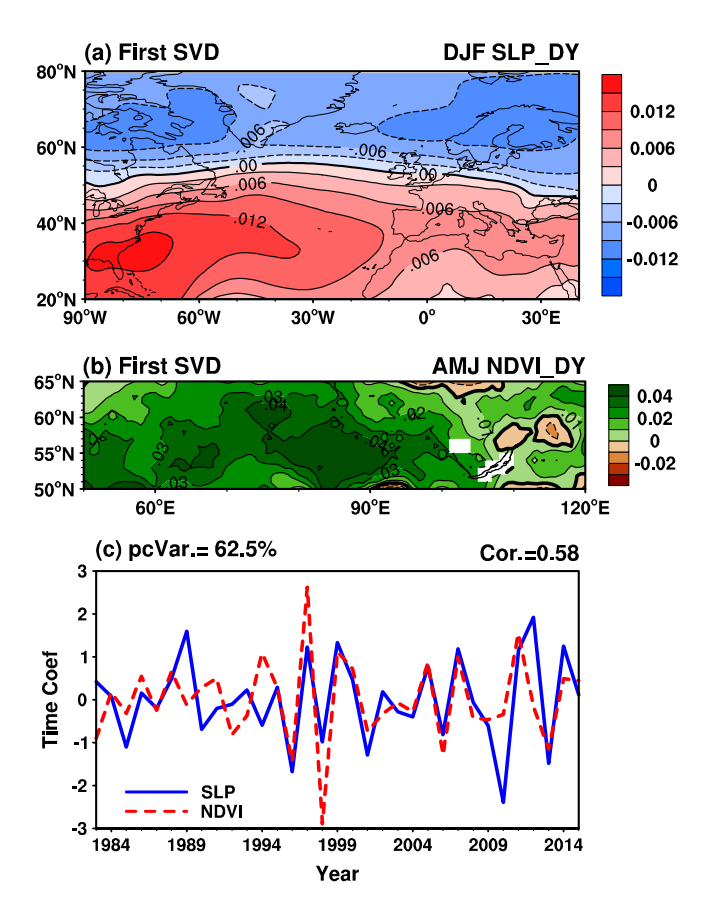


Figure 6. Spatial patterns for the first paired mode of the DY of (a) winter (December–January–February (DJF)) sea surface temperature (SST, tropical Pacific) and (b) spring (April–May–June (AMJ)) NDVIEA via SVD analysis during 1983–2015. (c) The corresponding normalized time series of the expansion coefficients for the paired mode; their correlation coefficient is shown above the top right-hand corner, and the variance explained by the first mode is shown above the top left-hand corner.

In positive-phase winter NAO years, there are cyclonic circulation anomalies over the northern part of the North Atlantic and anticyclonic circulation anomalies over the southern part. In turn, due to the propagation of Rossby waves originating from the Novaya Zemlya, anticyclonic circulation anomalies

are excited in a region centered near Lake Baikal [23]. Therefore, the corresponding anomalous westerly winds from the wet and warm Atlantic can lead to increases in surface air temperature and decreases in snow water over Eurasia. In the following spring, the corresponding thinner snow cover melts rapidly and Eurasian soil temperatures show positive anomalies because of the lower surface albedo and reduced latent heat from the snowmelt. Therefore, NDVIEA shows higher than normal values in spring following positive-phase winter NAO. Thus, the sea level pressure over (20°–80°N, 90W°–40°E) was used in the prediction of NDVIEA.

In summary, four predictors were identified: Spring SAT-CFS (40°-70°N, 30°-130°E); winter SICBS (78°-85°N, 25°-130°E); winter SSTP (20°S-20°N, 140E°-70°W); and winter NAO (sea level pressure over (20°-80°N, 90°W-40°E)). Each of the four predictors represent a physical connection relative to spring NDVIEA. Meanwhile, the correlation coefficients between the time series of expansion coefficients corresponding to the first SVD mode between the predictand and predictors are significant at the 1% significance level. Therefore, prediction schemes were developed based on these predictors.

3.2. Verification of the Prediction Schemes

3.2.1. Cross-Validation

Four single-predictor hindcast schemes based on each predictor were explored (i.e., the SAT-CFS scheme, SICBS scheme, SSTP scheme, and NAO scheme). Meanwhile, the NDVIEA results from the three previous-season single-predictor schemes (i.e., SICBS, SSTP and NAO) were considered in a statistical scheme via multiple linear regression, in which different stations have different weights. Furthermore, a hybrid scheme was developed based on the one synchronous predictor scheme from CFSv2 and the three previous-season predictor schemes (i.e., SAT-CFS, SICBS, SSTP, and NAO).

At each grid point, the temporal correlation coefficients (TCCs) for the SAT-CFS scheme, SICBS scheme, SSTP scheme, and NAO scheme are shown in Figure 7. Of all the 1130 grid points, the TCCs between the cross-validation and satellite data of NDVI are statistically significant at the 5% significance level at 686, 608, 819 and 624 grid points, which account for 61%, 54%, 73% and 55% of the total grid points, respectively (Table 1). The averaged TCCs for the single-predictor schemes are 0.38, 0.36, 0.43 and 0.36, respectively, which are all significant at the 5% significance level. The TCCs between the NDVI3g data and the cross-validation results of the statistical scheme and the hybrid scheme are significant at the 5% significance level at 977 and 1033 grid points, which account for 87% and 92% of the total grid points, respectively (Table 1, Figure 7). The averaged TCCs for them are 0.51 (significant at the 1% significance level) and 0.55 (significant at the 0.1% significance level), respectively. In the hybrid scheme, the TCCs at almost all the grid points (96% of the grid points) are significant at the 10% significance level. Meanwhile, the averaged temporal RMSEs at each grid point were calculated (Table 1). The single-predictor schemes show relatively higher temporal RMSE (0.07, 0.08, 0.07 and 0.08, respectively), while the hybrid scheme and the statistical scheme show the least error (0.04, Table 1).

The time series of spatial correlation coefficients (SCCs) between the satellite NDVI3g data and the results of the schemes are also presented (Figure 8). For the single-predictor scheme, the SCCs in most of the years are significant at the 1% significance level (0.08) during 1983–2015, except for 1991 and 2015 in the NAO scheme and 1996 in the SICBS scheme. The SCCs of the statistical scheme and the hybrid scheme are significant at the 1% significance level in all the years throughout 1983 to 2015. The multi-year averaged SCC for each scheme is presented and the hybrid scheme shows the highest averaged SCC (0.60, Table 1). Therefore, the hybrid scheme, which combines the synchronous spring predictor with the previous-season predictors, shows the highest prediction skill in terms of the spatiotemporal distribution and amplitude of the temporal variability.

Tabla 1	Comparison of the	cross-validation result	e of the	prediction	echamae	for NDVIEA
Table 1.	Companison of the	C1055-vanuation result	s or the	prediction	scriemes	IOI IND VIEA.

Scheme	Predictor(s)	TCC Percentage	SCC	RMSE
SAT-CFS Scheme	SAT-CFS	61%	0.46	0.07
SICBS Scheme	SICBS	54%	0.40	0.08
SSTP Scheme	SSTP	73%	0.48	0.07
NAO Scheme	NAO	55%	0.38	0.08
Statistical Scheme	SICBS, SSTP, NAO	87%	0.57	0.04
Hybrid Scheme	SICBS, SSTP, NAO, SAT-CFS	92%	0.60	0.04

Notes: TCC percentage: the percentage of grid points where the temporal correlation coefficients are significant at the 5% significance level; SCC: the averaged spatial correlation coefficient during 1983–2015; RMSE: the averaged root-mean-square-error of all the grids.

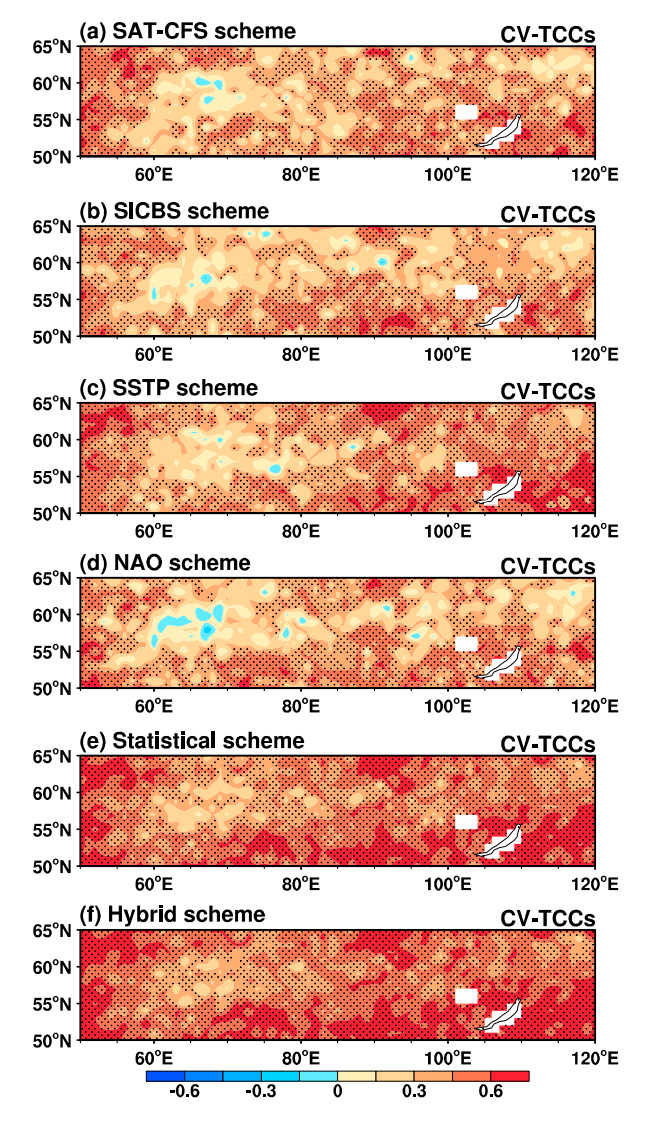


Figure 7. The temporal correlation coefficients (TCCs) between the spring (April–May–June (AMJ)) NDVI3g data and the cross-validation hindcast results of the (a) surface air temperature (SAT-CFS) scheme, (b) sea-ice cover (SIC) scheme, (c) sea surface temperature (SSTP) scheme, (d) North Atlantic Oscillation (NAO) scheme, (e) statistical scheme and (f) hybrid scheme during 1983–2015. Dotted regions are significant ($\alpha = 0.05$; t-test).

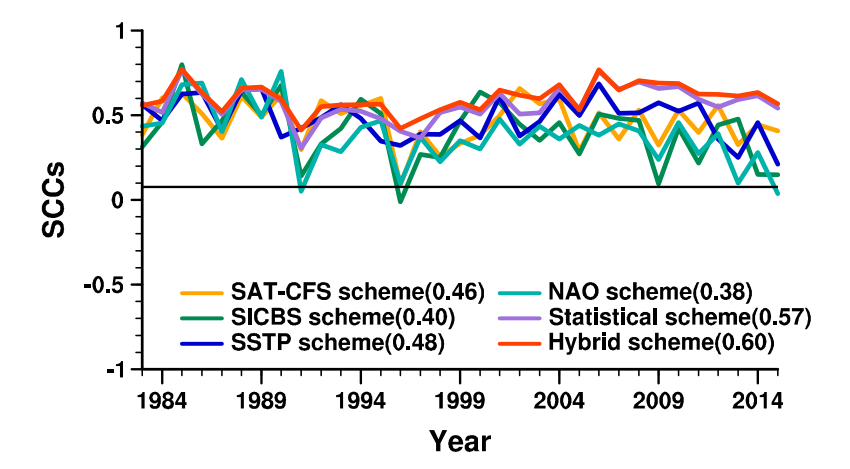


Figure 8. The spatial correlation coefficients (SCCs) between the spring (April–May–June (AMJ)) NDVI3g data and the cross-validation hindcast results of the schemes during 1983–2015. The reference line is the significant value for SCCs at the 1% significance level. Numbers in brackets in the legends are the averaged SCCs for the schemes during 1983–2015.

3.2.2. Independent Hindcast

Due to the good performance of the hybrid scheme in the cross-validation results, independent hindcasts for the period 2010–2015 were performed based on the hybrid scheme to further verify its prediction skill. Figure 9 depicts the distribution of NDVI3g values and the results of the hybrid scheme during 2010–2015. In general, the spatial distribution of the NDVI differences between the relatively high values over the West Siberian Plain (around 55°–65°N, 60°–100°E) and the East European Plain (around 50°–65°N, 50°–60°E), and the relatively low values over the Kazakh Uplands (around 50°–55°N, 60°–80°E) and the Stanovoy Range (east of the Lake Baikal), are well predicted (Figure 9). Meanwhile, the hybrid scheme captures the features of the interannual variability of NDVIEA during 2010–2015 (Figures 9 and 10). For example, in 2010 and 2012, the positive anomalies of NDVI values over the East European Plain are predicted by the hybrid scheme. Both the NDVI3g data and the hybrid scheme results show negative anomalies of NDVI over the West Siberian Plain in 2010, 2013 and 2014, and positive anomalies of NDVI in 2011, 2012 and 2015. The negative anomalies of NDVI values over the Stanovoy Range in 2010, 2012 and 2015, and positive anomalies of NDVI values in 2011, 2013 and 2014, are also well predicted by the hybrid scheme.

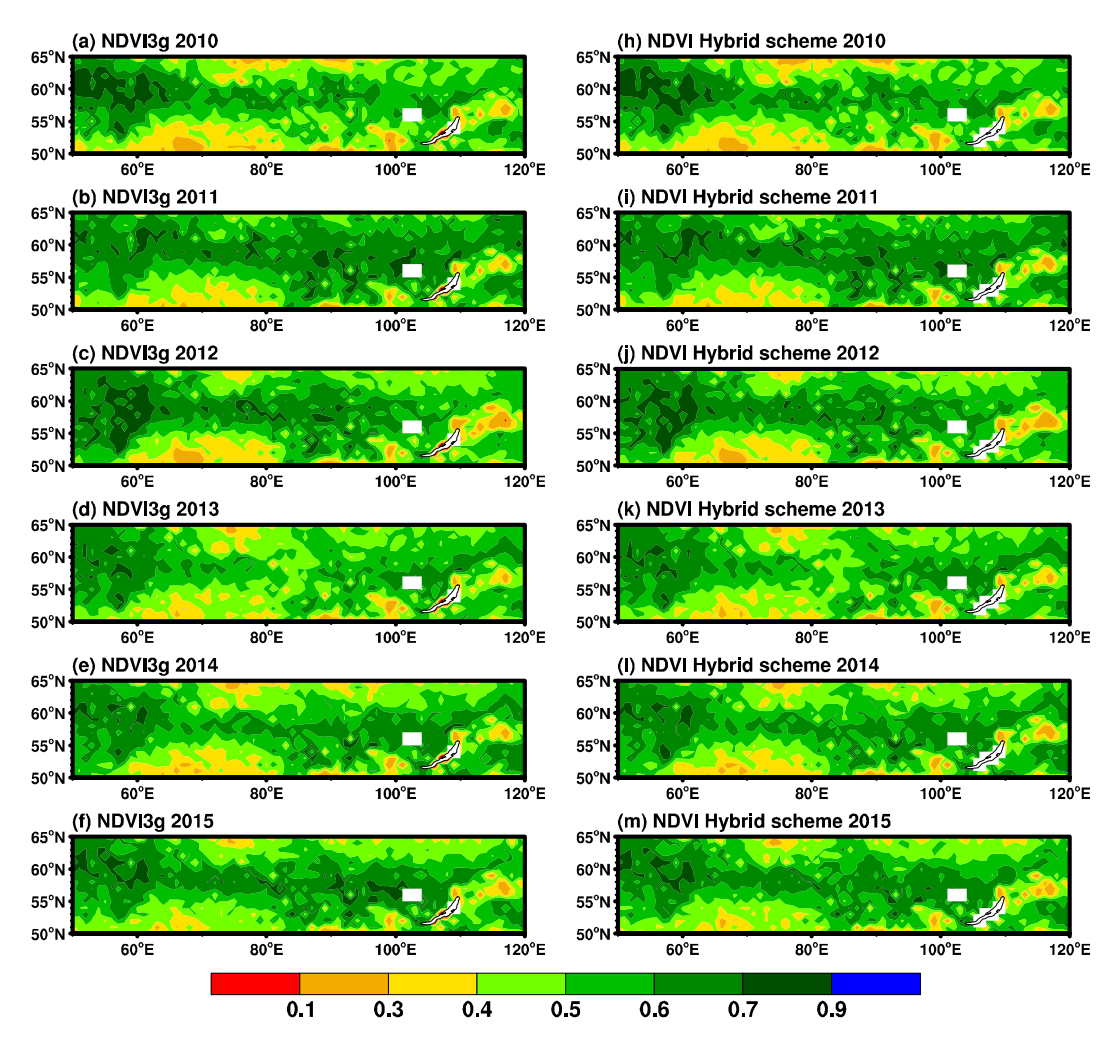


Figure 9. Spring (April–May–June (AMJ)) NDVI over Eurasia during 2010–2015, where (**a–f**) are from the NDVI3g data and (**h–m**) are from the independent hindcast results of the hybrid scheme.

Remote Sens. 2019, 11, 2123 15 of 21

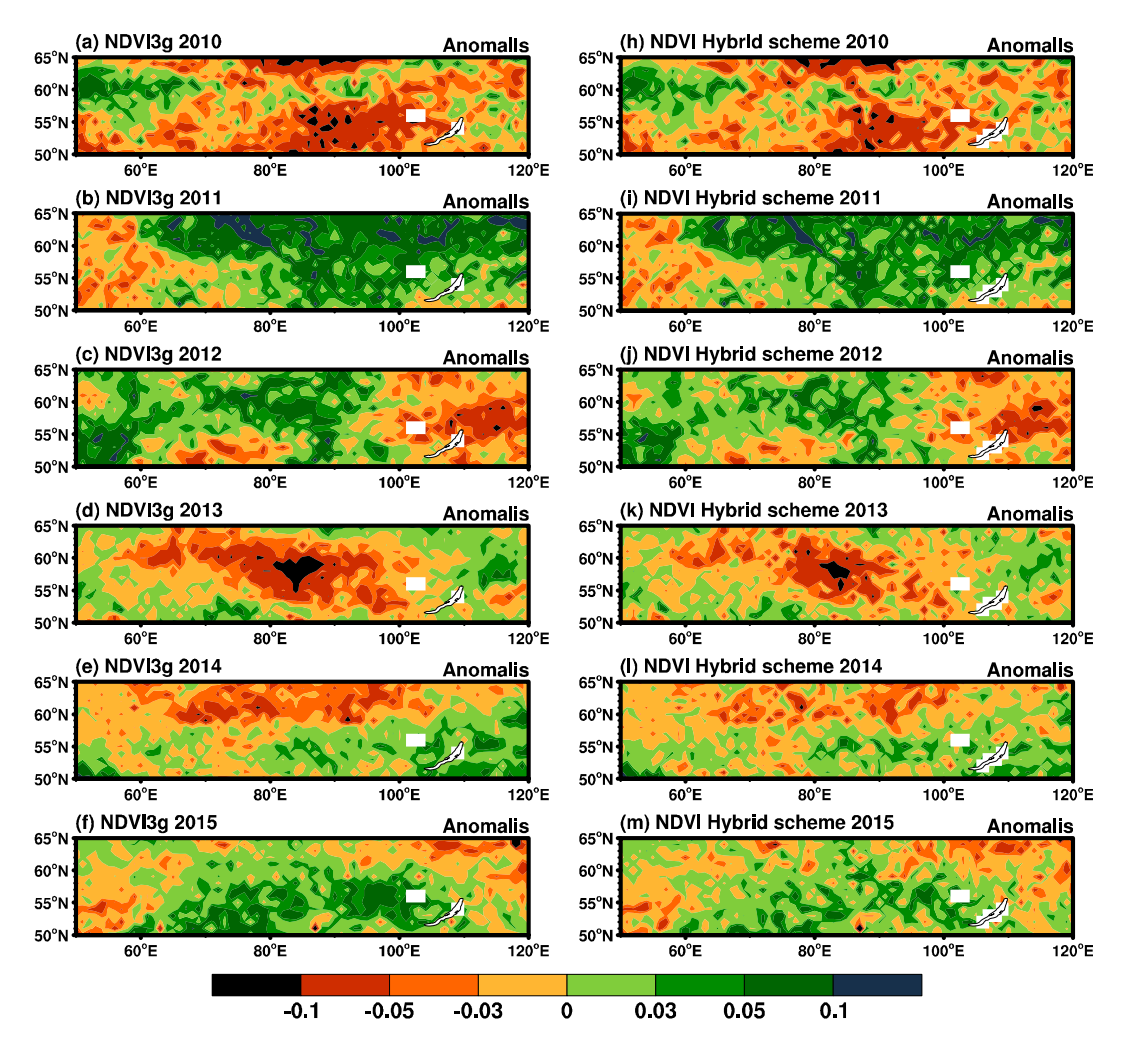


Figure 10. Spring (April–May–June (AMJ)) NDVI anomalies over Eurasia during 2010–2015, where (**a–f**) are from the NDVI3g data and (**h–m**) are from the independent hindcast results of the hybrid scheme.

4. Discussion

Vegetation plays an important role in the interaction between ecosystems and the atmosphere, and has gained much attention in recent years. To represent the vegetation dynamics at the global scale, the dynamic global vegetation models (DGVMs) have been developed [101]. Although these DGVMs are able to roughly simulate the distribution of global vegetation types and the equilibrium of ecosystems, it is hard for them to predict the evolution of terrestrial vegetation under the current global climate change situation [102,103]. Therefore, statistical climate predictions based on satellite-based vegetation data, applying local weather and climate predictors, have been developed [40-42]. For instance, Fu, et al. [41] developed a multiple linear regression model to predict NDVI over the Heihe River Basin in China based on local precipitation, temperature, and soil moisture in each grid cell. The model showed high prediction skill over the regions where the NDVI was highly correlated with local precipitation, temperature, and soil moisture. However, the prediction skill showed a need for improvement over the regions where the NDVI was not significantly related to the local predictors. Given that large-scale climate patterns provide a conceptual framework and a broader understanding of observed changes in the local physical environment, large-scale climate indices seem to be better predictors of ecological processes than local climate [45–47]. Therefore, This study focused on developing a climate prediction model based on the coupled spatiotemporal patterns between the Eurasian NDVI and large-scale as well as local climate factors. The coupled spatiotemporal patterns between NDVI and the different predictors enable the prediction models to capture the spatiotemporal variability of NDVI effectively,

which improves the prediction skill compared with multiple linear regression models, especially over the regions where the NDVI is not significantly related to the local predictors [59,104–107].

In this work, cross-validation and independent hindcast results indicate that the year-to-year increment schemes are able to predict NDVIEA effectively, especially the hybrid model. The hybrid scheme performs better than the single-predictor schemes and the statistical scheme because of its comprehensive consideration of the previous-season signals of the sea and atmosphere and the synchronous atmospheric signal derived from the CFSv2 dynamic climate prediction model. The skillful prediction of NDVIEA uncovered in this study can be seen as an important reference for the evolution of vegetation dynamics, and is helpful for our understanding of the Eurasian climate and environment.

Nevertheless, there is still room for improvement in terms of the prediction skill over some regions where the TCCs are not significant. This improvement could be achieved in future work in several respects. Firstly, with the development of dynamic climate prediction models, it may be possible to incorporate more synchronous climatic predictors, such as precipitation and soil moisture, to further improve the prediction skill. Meanwhile, other processes that are not directly linked with climate can also influence the Eurasian NDVI, such as land use, land cover change, pests, and so on [108–110]. How to incorporate these factors into the NDVI prediction models needs to be investigated in future work.

Eurasia is the largest continent, covering more than 30% of Earth's total land area. This study focused on the region where the first spatial mode of the EOF pattern of NDVI shows the largest values in the middle to high latitudes, which means significant variations of NDVI. However, other regions in the middle to high latitudes over Eurasia may be affected by different climate factors. For example, Li et al. [96] found that the NDVI in Western Europe is strongly related to Central Pacific Niño events, whereas the NDVI in East Russia is significantly influenced by Eastern Pacific Niño events. Gong and Shi [111] found that large-scale climate signals could exert different influences on the interannual variations of Eurasian spring vegetation greenness from region to region. For example, for the NDVI over Eastern Europe, the Southern Oscillation dominates over other factors, whereas the Eurasian pattern is the most important atmospheric system for West Siberia. Therefore, future work is needed to expand the area of the prediction model.

5. Conclusions

Seasonal climate prediction schemes of spring vegetation over Eurasia were developed using the year-to-year increment approach. The prediction schemes are based on the coupled spatiotemporal patterns between NDVIEA and relevant climate factors. First, the local spring surface air temperature was found to be a dominant factor for NDVIEA. However, observational or reanalysis data for this factor are unavailable in advance. Thus, the surface air temperature derived from the CFSv2 dynamic climate prediction model was applied as a synchronous predictor (SAT-CFS). Meanwhile, the winter sea-ice cover over the Barents Sea (referred to as SICBS), the winter sea surface temperature over the equatorial Pacific (referred to as SSTP), and winter NAO, all have effects on NDVIEA via different teleconnections. Therefore, they too were considered, as three previous-season predictors.

Four single-predictor schemes (i.e., the SAT-CFS scheme, SICBS scheme, SSTP scheme, and NAO scheme) were proposed, as well as a statistical scheme comprising SICBS, SSTP and NAO, and a hybrid scheme that included all four predictors. The one-year-out cross-validation and independent hindcasts were performed to evaluate their prediction skills. For the cross-validation results, in general, all the schemes show high skill in predicting NDVIEA. For all six schemes, the TCCs of more than 50% of the grid points are significant at the 5% significance level. Meanwhile, the SCCs of the six schemes are significant at the 1% significance level in almost all years during 1983–2015. Among them, the hybrid scheme performs better than the other schemes, with higher TCCs (0.55) and SCCs (0.60). Meanwhile, the RMSE of the hybrid scheme is the least amongst the schemes (0.04). The independent hindcast of the hybrid scheme was performed during 2010–2015, and the results compared with the NDVI3g data. It can be concluded that the hybrid scheme can capture both the spatial and the temporal variability of NDVIEA.

Remote Sens. 2019, 11, 2123 17 of 21

Author Contributions: K.F. conceived and designed the experiments and the paper; L.J. performed the experiments, analyzed the data and wrote the paper.

Funding: This research was supported by the National Natural Science Foundation of China (grants 41730964, 41421004, and 41575079).

Conflicts of Interest: The authors declare no conflicts of interest.

References

- 1. IPCC. Climate Change 2013: The Physical Science Basis. Contribution of Working Group I to the Fifth Assessment Report of the Intergovernmental Panel on Climate Change; Stocker, T.F., Qin, D., Plattner, G.-K., Tignor, M., Allen, S.K., Boschung, J., Nauels, A., Xia, Y., Bex, V., Midgley, P.M., Eds.; Cambridge University Press: Cambridge, UK, 2013. [CrossRef]
- 2. Myneni, R.B.; Keeling, C.D.; Tucker, C.J.; Asrar, G.; Nemani, R.R. Increased plant growth in the northern high latitudes from 1981 to 1991. *Nature* **1997**, *386*, 698. [CrossRef]
- 3. Keeling, C.D.; Chin, J.F.S.; Whorf, T.P. Increased activity of northern vegetation inferred from atmospheric CO2 measurements. *Nature* **1996**, *382*, 146. [CrossRef]
- 4. Nemani, R.R.; Keeling, C.D.; Hashimoto, H.; Jolly, W.M.; Piper, S.C.; Tucker, C.J.; Myneni, R.B.; Running, S.W. Climate-Driven Increases in Global Terrestrial Net Primary Production from 1982 to 1999. *Science* 2003, 300, 1560–1563. [CrossRef] [PubMed]
- 5. Bogaert, J.; Zhou, L.; Tucker, C.J.; Myneni, R.B.; Ceulemans, R. Evidence for a persistent and extensive greening trend in Eurasia inferred from satellite vegetation index data. *J. Geophys. Res. Atmos.* **2002**, 107, ACL 4-1–ACL 4-14. [CrossRef]
- 6. Dye, D.G.; Tucker, C.J. Seasonality and trends of snow-cover, vegetation index, and temperature in northern Eurasia. *Geophys. Res. Lett.* **2003**, *30*. [CrossRef]
- 7. Yue, X.; Unger, N.; Keenan, T.F.; Zhang, X.; Vogel, C.S. Probing the past 30-year phenology trend of US deciduous forests. *Biogeosciences* **2015**, 12, 4693–4709. [CrossRef]
- 8. Betts, R.A.; Cox, P.M.; Lee, S.E.; Woodward, F.I. Contrasting physiological and structural vegetation feedbacks in climate change simulations. *Nature* **1997**, *387*, 796–799. [CrossRef]
- 9. Jiang, D.B.; Zhang, Y.; Lang, X.M. Vegetation feedback under future global warming. *Theor. Appl. Climatol.* **2011**, *106*, 211–227. [CrossRef]
- 10. Milly, P.C.D.; Dunne, K.A. Sensitivity of the global water cycle to the water-holding capacity of land. *J. Clim.* **1994**, 7, 506–526. [CrossRef]
- 11. Gallimore, R.G.; Kutzbach, J.E. Role of orbitally induced changes in tundra area in the onset of glaciation. *Nature* **1996**, *381*, 503–505. [CrossRef]
- 12. Mahmood, R.; Pielke, R.A.; Hubbard, K.G.; Niyogi, D.; Dirmeyer, P.A.; McAlpine, C.; Carleton, A.M.; Hale, R.; Gameda, S.; Beltrán-Przekurat, A.; et al. Land cover changes and their biogeophysical effects on climate. *Int. J. Climatol.* **2014**, 34, 929–953. [CrossRef]
- 13. Richardson, A.D.; Keenan, T.F.; Migliavacca, M.; Ryu, Y.; Sonnentag, O.; Toomey, M. Climate change, phenology, and phenological control of vegetation feedbacks to the climate system. *Agric. Forest Meteorol.* **2013**, *169*, 156–173. [CrossRef]
- 14. Sun, B.; Wang, H. Moisture Sources of Semiarid Grassland in China Using the Lagrangian Particle Model FLEXPART. *J. Clim.* **2014**, 27, 2457–2474. [CrossRef]
- 15. Bonan, G.B.; Chapin, F.S.; Thompson, S.L. Boreal forest and tundra ecosystems as components of the climate system. *Clim. Chang.* **1995**, *29*, 145–167. [CrossRef]
- 16. MacDonald, G.M.; Kremenetski, K.V.; Beilman, D.W. Climate change and the northern Russian treeline zone. *Philos. T. R. Soc. B* **2008**, *363*, 2283–2299. [CrossRef] [PubMed]
- 17. Snyder, P.K.; Delire, C.; Foley, J.A. Evaluating the influence of different vegetation biomes on the global climate. *Clim. Dyn.* **2004**, *23*, 279–302. [CrossRef]
- 18. Mao, R.; Gong, D.Y.; Deliang, C. The evident linkage of springtime NDVI over Eurasia with East Asian atmospheric circulation in summer. *Acta Meteorol. Sin.* **2008**, 592–598. [CrossRef]
- 19. Bonan, G.B.; Pollard, D.; Thompson, S.L. Effects of boreal forest vegetation on global climate. *Nature* **1992**, 359, 716. [CrossRef]
- 20. Thomas, G.; Rowntree, P.R. The Boreal Forests and Climate. Q. J. R. Meteor. Soc. 1992, 118, 469–497. [CrossRef]

Remote Sens. 2019, 11, 2123 18 of 21

21. Pearson, R.G.; Phillips, S.J.; Loranty, M.M.; Beck, P.S.A.; Damoulas, T.; Knight, S.J.; Goetz, S.J. Shifts in Arctic vegetation and associated feedbacks under climate change. *Nat. Clim. Chang.* **2013**, *3*, 673. [CrossRef]

- 22. Yue, X.; Unger, N.; Zheng, Y. Distinguishing the drivers of trends in land carbon fluxes and plant volatile emissions over the past 3 decades. *Atmos. Chem. Phys.* **2015**, *15*, 11931–11948. [CrossRef]
- 23. Li, J.; Fan, K.; Xu, Z. Links between the late wintertime North Atlantic Oscillation and springtime vegetation growth over Eurasia. *Clim. Dyn.* **2016**, *46*, 987–1000. [CrossRef]
- 24. Piao, S.; Ciais, P.; Friedlingstein, P.; Peylin, P.; Reichstein, M.; Luyssaert, S.; Margolis, H.; Fang, J.; Barr, A.; Chen, A.; et al. Net carbon dioxide losses of northern ecosystems in response to autumn warming. *Nature* **2008**, *451*, 49. [CrossRef] [PubMed]
- 25. Black, T.A.; Chen, W.J.; Barr, A.G.; Arain, M.A.; Chen, Z.; Nesic, Z.; Hogg, E.H.; Neumann, H.H.; Yang, P.C. Increased carbon sequestration by a boreal deciduous forest in years with a warm spring. *Geophys. Res. Lett.* **2000**, *27*, 1271–1274. [CrossRef]
- 26. Siegmann, B.; Jarmer, T. Comparison of different regression models and validation techniques for the assessment of wheat leaf area index from hyperspectral data. *Int. J. Remote Sens.* **2015**, *36*, 4519–4534. [CrossRef]
- 27. Zhang, K.; Ge, X.; Shen, P.; Li, W.; Liu, X.; Cao, Q.; Zhu, Y.; Cao, W.; Tian, Y. Predicting Rice Grain Yield Based on Dynamic Changes in Vegetation Indexes during Early to Mid-Growth Stages. *Remote Sens.* **2019**, *11*, 387. [CrossRef]
- 28. Quarmby, N.A.; Milnes, M.; Hindle, T.L.; Silleos, N. The use of multi-temporal NDVI measurements from AVHRR data for crop yield estimation and prediction. *Int. J. Remote Sens.* **1993**, *14*, 199–210. [CrossRef]
- 29. Kanning, M.; Kühling, I.; Trautz, D.; Jarmer, T. High-Resolution UAV-Based Hyperspectral Imagery for LAI and Chlorophyll Estimations from Wheat for Yield Prediction. *Remote Sens.* **2018**, *10*, 2000. [CrossRef]
- 30. Sun, L.; Gao, F.; Anderson, M.C.; Kustas, W.P.; Alsina, M.M.; Sanchez, L.; Sams, B.; McKee, L.; Dulaney, W.; White, W.A.; et al. Daily Mapping of 30 m LAI and NDVI for Grape Yield Prediction in California Vineyards. *Remote Sens.* **2017**, *9*, 317. [CrossRef]
- 31. Prasad, A.K.; Chai, L.; Singh, R.P.; Kafatos, M. Crop yield estimation model for Iowa using remote sensing and surface parameters. *Int. J. Appl. Earth Obs. Geoinf.* **2006**, *8*, 26–33. [CrossRef]
- 32. Dutta, D.; Kundu, A.; Patel, N.R. Predicting agricultural drought in eastern Rajasthan of India using NDVI and standardized precipitation index. *Geocarto Int.* **2013**, *28*, 192–209. [CrossRef]
- 33. Karnieli, A.; Agam, N.; Pinker, R.T.; Anderson, M.; Imhoff, M.L.; Gutman, G.G.; Panov, N.; Goldberg, A. Use of NDVI and Land Surface Temperature for Drought Assessment: Merits and Limitations. *J. Clim.* **2010**, 23, 618–633. [CrossRef]
- 34. Anyamba, A.; Tucker, C.J. Analysis of Sahelian vegetation dynamics using NOAA-AVHRR NDVI data from 1981–2003. *J. Arid Environ.* **2005**, *63*, 596–614. [CrossRef]
- 35. Anyamba, A.; Small, J.; Tucker, C.; Pak, E. Thirty-two Years of Sahelian Zone Growing Season Non-Stationary NDVI3g Patterns and Trends. *Remote Sens.* **2014**, *6*, 3101. [CrossRef]
- 36. Mueller, T.; Dressler, G.; Tucker, C.; Pinzon, J.; Leimgruber, P.; Dubayah, R.; Hurtt, G.; Böhning-Gaese, K.; Fagan, W. Human Land-Use Practices Lead to Global Long-Term Increases in Photosynthetic Capacity. *Remote Sens.* **2014**, *6*, 5717. [CrossRef]
- 37. Scheftic, W.; Zeng, X.; Broxton, P.; Brunke, M. Intercomparison of Seven NDVI Products over the United States and Mexico. *Remote Sens.* **2014**, *6*, 1057. [CrossRef]
- 38. Tucker, C.J. Red and photographic infrared linear combinations for monitoring vegetation. *Remote Sens. Environ.* **1979**, *8*, 127–150. [CrossRef]
- 39. Myneni, R.B.; Hall, F.G.; Sellers, P.J.; Marshak, A.L. The interpretation of spectral vegetation indexes. *IEEE Trans. Geosci. Remote* **1995**, *33*, 481–486. [CrossRef]
- 40. Iwasaki, H. NDVI prediction over Mongolian grassland using GSMaP precipitation data and JRA-25/JCDAS temperature data. *J. Arid Environ.* **2009**, *73*, 557–562. [CrossRef]
- 41. Fu, J.; Niu, J.; Sivakumar, B. Prediction of vegetation anomalies over an inland river basin in north-western China. *Hydrol. Process.* **2018**, 32, 1814–1827. [CrossRef]
- 42. Martiny, N.; Philippon, N.; Richard, Y.; Camberlin, P.; Reason, C. Predictability of NDVI in semi-arid African regions. *Theor. Appl. Climatol.* **2010**, 100, 467–484. [CrossRef]
- 43. Gurung, R.B.; Breidt, F.J.; Dutin, A.; Ogle, S.M. Predicting Enhanced Vegetation Index (EVI) curves for ecosystem modeling applications. *Remote Sens. Environ.* **2009**, *113*, 2186–2193. [CrossRef]

Remote Sens. 2019, 11, 2123 19 of 21

44. Roerink, G.J.; Menenti, M.; Soepboer, W.; Su, Z. Assessment of climate impact on vegetation dynamics by using remote sensing. *Phys. Chem. Earth Parts A B C* **2003**, *28*, 103–109. [CrossRef]

- 45. Hallett, T.B.; Coulson, T.; Pilkington, J.G.; Clutton-Brock, T.H.; Pemberton, J.M.; Grenfell, B.T. Why large-scale climate indices seem to predict ecological processes better than local weather. *Nature* **2004**, *430*, 71–75. [CrossRef] [PubMed]
- 46. Stenseth Nils, C.; Ottersen, G.; Hurrell James, W.; Mysterud, A.; Lima, M.; Chan, K.S.; Yoccoz Nigel, G.; Ådlandsvik, B. Review article. Studying climate effects on ecology through the use of climate indices: The North Atlantic Oscillation, El Niño Southern Oscillation and beyond. Proceedings of the Royal Society of London. *Ser. B Biol. Sci.* 2003, 270, 2087–2096. [CrossRef] [PubMed]
- 47. Bastos, A.; Ciais, P.; Park, T.; Zscheischler, J.; Yue, C.; Barichivich, J.; Myneni, R.B.; Peng, S.; Piao, S.; Zhu, Z. Was the extreme Northern Hemisphere greening in 2015 predictable? *Environ. Res. Lett.* **2017**, *12*, 044016. [CrossRef]
- 48. Los, S.O.; Collatz, G.J.; Bounoua, L.; Sellers, P.J.; Tucker, C.J. Global Interannual Variations in Sea Surface Temperature and Land Surface Vegetation, Air Temperature, and Precipitation. *J. Clim.* **2001**, *14*, 1535–1549. [CrossRef]
- 49. Schultz, P.A.; Halpert, M.S. Global correlation of temperature, NDVI and precipitation. *Adv. Space Res.* **1993**, 13, 277–280. [CrossRef]
- 50. Zhang, X.; Friedl, M.A.; Schaaf, C.B.; Strahler, A.H. Climate controls on vegetation phenological patterns in northern mid- and high latitudes inferred from MODIS data. *Glob. Chang. Biol.* **2004**, *10*, 1133–1145. [CrossRef]
- 51. Barichivich, J.; Briffa, K.; Myneni, R.; Schrier, G.; Dorigo, W.; Tucker, C.; Osborn, T.; Melvin, T. Temperature and Snow-Mediated Moisture Controls of Summer Photosynthetic Activity in Northern Terrestrial Ecosystems between 1982 and 2011. *Remote Sens.* **2014**, *6*, 1390. [CrossRef]
- 52. Li, J.; Fan, K.; Xu, Z. Asymmetric response in Northeast Asia of summer NDVI to the preceding ENSO cycle. *Clim. Dyn.* **2016**, *47*, 2765–2783. [CrossRef]
- 53. Ji, L.; Fan, K. Interannual linkage between wintertime sea-ice cover variability over the Barents Sea and springtime vegetation over Eurasia. *Clim. Dyn.* **2019**, 1–16. [CrossRef]
- 54. Li, J.; Fan, K.; Xu, J.; Powell, A.M., Jr.; Kogan, F. The effect of preceding wintertime Arctic polar vortex on springtime NDVI patterns in boreal Eurasia, 1982–2015. *Clim. Dyn.* **2017**, *49*, 23–35. [CrossRef]
- 55. Fan, K.; Liu, Y.; Chen, H.P. Improving the prediction of the East Asian summer monsoon: New approaches. *Weather Forecast.* **2012**, 27, 1017–1030. [CrossRef]
- 56. Liu, Y.; Fan, K. An application of hybrid downscaling model to forecast summer precipitation at stations in China. *Atmos. Res.* **2014**, *143*, 17–30. [CrossRef]
- 57. Ji, L.; Fan, K. Climate prediction of dust weather frequency over northern China based on sea-ice cover and vegetation variability. *Clim. Dyn.* **2019**, *53*, 687–705. [CrossRef]
- 58. Bretherton, C.S.; Smith, C.; Wallace, J.M. An intercomparison of methods for finding coupled patterns in climate data. *J. Clim.* **1992**, *5*, 541–560. [CrossRef]
- 59. Chu, J.-L.; Kang, H.; Tam, C.-Y.; Park, C.-K.; Chen, C.-T. Seasonal forecast for local precipitation over northern Taiwan using statistical downscaling. *J. Geophys. Res.-Atmos.* **2008**, *113*. [CrossRef]
- 60. Dai, H.; Fan, K.; Tian, B. A hybrid downscaling model for winter temperature over northeast China. *Int. J. Climatol.* **2018**, *38*, E349–E363. [CrossRef]
- 61. Fan, K.; Wang, H.J.; Choi, Y.-J. A physically-based statistical forecast model for the middle-lower reaches of the Yangtze River Valley summer rainfall. *Chin. Sci. Bull.* **2008**, *53*, 602–609. [CrossRef]
- 62. Tian, B.; Fan, K.; Yang, H. East Asian winter monsoon forecasting schemes based on the NCEP's climate forecast system. *Clim. Dyn.* **2018**, *51*, 2793–2805. [CrossRef]
- 63. Wang, H.J.; Zhang, Y.; Lang, X.M. On the predictand of short-term climate prediction. *Clim. Environ. Res.* **2010**, *15*, 225–228. [CrossRef]
- 64. Fan, K. A prediction model for Atlantic named storm frequency ysing a year-by-year increment approach. *Weather Forecast.* **2010**, *25*, 1842–1851. [CrossRef]
- 65. Fan, K.; Wang, H.J. A new approach to forecasting typhoon frequency over the western North Pacific. *Weather Forecast.* **2009**, *24*, 974–986. [CrossRef]

Remote Sens. 2019, 11, 2123 20 of 21

66. Kogan, F.; Guo, W.; Jelenak, A. Global Vegetation Health: Long-Term Data Records. In *Use of Satellite and in-Situ Data to Improve Sustainability*; Kogan, F., Powell, A.M., Fedorov, O., Eds.; Springer: Cham, Switzerland, 2011; 28p.

- 67. Pettorelli, N.; Vik, J.O.; Mysterud, A.; Gaillard, J.-M.; Tucker, C.J.; Stenseth, N.C. Using the satellite-derived NDVI to assess ecological responses to environmental change. *Trends Ecol. Evol.* **2005**, *20*, 503–510. [CrossRef] [PubMed]
- 68. Bannari, A.; Morin, D.; Bonn, F.; Huete, A.R. A review of vegetation indices. *Remote Sens. Rev.* **1995**, *13*, 95–120. [CrossRef]
- 69. Myneni, R.B.; Williams, D.L. On the relationship between FAPAR and NDVI. *Remote Sens. Environ.* **1994**, 49, 200–211. [CrossRef]
- 70. Li, A.; Liang, S.; Wang, A.; Huang, C. Investigating the impacts of the North Atlantic Oscillation on global vegetation changes by a remotely sensed vegetation index. *Int. J. Remote Sens.* **2012**, *33*, 7222–7239. [CrossRef]
- 71. Mennis, J. Exploring relationships between ENSO and vegetation vigour in the south-east USA using AVHRR data. *Int. J. Remote Sens.* **2001**, 22, 3077–3092. [CrossRef]
- 72. Pinzon, J.E.; Tucker, C.J. A Non-Stationary 1981-2012 AVHRR NDVI3g Time Series. *Remote Sens.* **2014**, *6*, 6929–6960. [CrossRef]
- 73. Dee, D.P.; Uppala, S.M.; Simmons, A.J.; Berrisford, P.; Poli, P.; Kobayashi, S.; Andrae, U.; Balmaseda, M.A.; Balsamo, G.; Bauer, P.; et al. The ERA-Interim reanalysis: Configuration and performance of the data assimilation system. *Q. J. R.; Meteor. Soc.* **2011**, *137*, 553–597. [CrossRef]
- 74. Rayner, N.A.; Parker, D.E.; Horton, E.B.; Folland, C.K.; Alexander, L.V.; Rowell, D.P.; Kent, E.C.; Kaplan, A. Global analyses of sea surface temperature, sea ice, and night marine air temperature since the late nineteenth century. *J. Geophys. Res.-Atmos* **2003**, *108*, 4407–4437. [CrossRef]
- 75. Armstrong, R.L.; Brodzik, M.J.; Knowles, K.; Savoie, M. *Global Monthly EASE-Grid Snow Water Equivalent Climatology*; National Snow and Ice Data Center: Boulder, CO, USA, 2007.
- 76. Robinson, D.A.; Dewey, K.F.; Heim, R.R. Global snow cover monitoring-an update. *B. Am. Meteorol. Soc.* **1993**, 74, 1689–1696. [CrossRef]
- 77. Barnston, A.G.; Livezey, R.E. Classification, Seasonality and Persistence of Low-Frequency Atmospheric Circulation Patterns. *Mon. Weather Rev.* **1987**, *115*, 1083–1126. [CrossRef]
- 78. Barnston, A.G.; Chelliah, M.; Goldenberg, S.B. Documentation of a highly ENSO-related sst region in the equatorial pacific: Research note. *Atmos. Ocean* **1997**, *35*, 367–383. [CrossRef]
- 79. Saha, S.; Moorthi, S.; Wu, X.; Wang, J.; Nadiga, S.; Tripp, P.; Behringer, D.; Hou, Y.-T.; Chuang, H.-Y.; Iredell, M.; et al. The NCEP Climate Forecast System Version 2. *J. Clim.* **2014**, 27, 2185–2208. [CrossRef]
- 80. Michaelsen, J. Cross-validation in statistical climate forcast models. *J. Clim. Appl. Meteorol.* **1987**, 26, 1589–1600. [CrossRef]
- 81. Takaya, K.; Nakamura, H. A formulation of a phase-independent wave-activity flux for stationary and migratory quasigeostrophic eddies on a zonally varying basic flow. *J. Atmos. Sci.* **2001**, *58*, 608–627. [CrossRef]
- 82. Ichii, K.; Kawabata, A.; Yamaguchi, Y. Global correlation analysis for NDVI and climatic variables and NDVI trends: 1982–1990. *Int. J. Remote Sens.* **2002**, *23*, 3873–3878. [CrossRef]
- 83. Park, H.-S.; Sohn, B.J. Recent trends in changes of vegetation over East Asia coupled with temperature and rainfall variations. *J. Geophys. Res.-Atmos.* **2010**, *115*. [CrossRef]
- 84. Tucker, C.J.; Slayback, D.A.; Pinzon, J.E.; Los, S.O.; Myneni, R.B.; Taylor, M.G. Higher northern latitude normalized difference vegetation index and growing season trends from 1982 to 1999. *Int. J. Biometeorol.* **2001**, *45*, 184–190. [CrossRef] [PubMed]
- 85. Serreze, M.C.; Holland, M.M.; Stroeve, J. Perspectives on the Arctic's shrinking sea-ice cover. *Science* **2007**, 315, 1533–1536. [CrossRef] [PubMed]
- 86. Vihma, T. Effects of arctic sea ice decline on weather and climate: A review. *Surv. Geophys.* **2014**, 35, 1175–1214. [CrossRef]
- 87. Cohen, J.; Screen, J.A.; Furtado, J.C.; Barlow, M.; Whittleston, D.; Coumou, D.; Francis, J.; Dethloff, K.; Entekhabi, D.; Overland, J.; et al. Recent Arctic amplification and extreme mid-latitude weather. *Nat. Geosci.* **2014**, *7*, 627–637. [CrossRef]
- 88. Wu, Q.; Cheng, L.; Chan, D.; Yao, Y.; Hu, H.; Yao, Y. Suppressed midlatitude summer atmospheric warming by Arctic sea ice loss during 1979–2012. *Geophys. Res. Lett.* **2016**, *43*, 2792–2800. [CrossRef]

Remote Sens. 2019, 11, 2123 21 of 21

89. Ellis, A.W.; Leathers, D.J. The effects of a discontinuous snow cover on lower atmospheric temperature and energy flux patterns. *Geophys. Res. Lett.* **1998**, 25, 2161–2164. [CrossRef]

- 90. Zuo, Z.Y.; Zhang, R.H.; Wu, B.Y.; Rong, X.Y. Decadal variability in springtime snow over Eurasia: Relation with circulation and possible influence on springtime rainfall over China. *Int. J. Climatol.* **2012**, 32, 1336–1345. [CrossRef]
- 91. Ogi, M.; Tachibana, Y.; Yamazaki, K. Impact of the wintertime North Atlantic Oscillation (NAO) on the summertime atmospheric circulation. *Geophys. Res. Lett.* **2003**, *30*. [CrossRef]
- 92. Rasmusson, E.M.; Wallace, J.M. Meteorological Aspects of the El Niño/Southern Oscillation. *Science* **1983**, 222, 1195–1202. [CrossRef]
- 93. Camp, C.D.; Tung, K.-K. Stratospheric polar warming by ENSO in winter: A statistical study. *Geophys. Res. Lett.* **2007**, 34. [CrossRef]
- 94. Gao, H.; Li, X. Influences of El Nino Southern Oscillation events on haze frequency in eastern China during boreal winters. *Int. J. Climatol.* **2015**, *35*, 2682–2688. [CrossRef]
- 95. Yang, X.-Q.; Xie, Q.; Ni, Y.-Q.; Huang, S.-S. ENSO cycle in a coupled ocean-atmosphere model and its negative feedback mechanism. *Meteorol. Atmos. Phys.* **1996**, *61*, 153–186. [CrossRef]
- 96. Li, J.; Fan, K.; Zhou, L.M. Satellite Observations of El Nino Impacts on Eurasian Spring Vegetation Greenness during the Period 1982–2015. *Remote Sens.* **2017**, *9*, 628. [CrossRef]
- 97. Xie, S.-P.; Hu, K.; Hafner, J.; Tokinaga, H.; Du, Y.; Huang, G.; Sampe, T. Indian Ocean Capacitor Effect on Indo–Western Pacific Climate during the Summer following El Niño. *J. Clim.* **2009**, 22, 730–747. [CrossRef]
- 98. Meyers, G.; McIntosh, P.; Pigot, L.; Pook, M. The Years of El Niño, La Niña, and Interactions with the Tropical Indian Ocean. *J. Clim.* **2007**, *20*, 2872–2880. [CrossRef]
- 99. Wu, R.; Kirtman, B.P.; Krishnamurthy, V. An asymmetric mode of tropical Indian Ocean rainfall variability in boreal spring. *J. Geophys. Res.-Atmos.* **2008**, *113*. [CrossRef]
- 100. Hurrell, J.W.; Kushnir, Y.; Ottersen, G.; Visbeck, M. An Overview of the North Atlantic Oscillation. *Geophys. Monogr.* **2003**, *134*, 1–35. [CrossRef]
- Quillet, A.; Peng, C.; Garneau, M. Toward dynamic global vegetation models for simulating vegetation-climate interactions and feedbacks: Recent developments, limitations, and future challenges. *Environ. Rev.* 2010, 18, 333–353. [CrossRef]
- 102. Zhu, J.; Zeng, X.; Zhang, M.; Dai, Y.; Ji, D.; Li, F.; Zhang, Q.; Zhang, H.; Song, X. Evaluation of the New Dynamic Global Vegetation Model in CAS-ESM. *Adv. Atmos. Sci.* **2018**, *35*, 659–670. [CrossRef]
- 103. Zeng, X.; Li, F.; Song, X. Development of the IAP Dynamic Global Vegetation Model. *Adv. Atmos. Sci.* **2014**, 31, 505–514. [CrossRef]
- 104. Feddersen, H.; Andersen, U. A method for statistical downscaling of seasonal ensemble predictions. *Tellus A Dyn. Meteorol. Oceanogr.* **2005**, *57*, 398–408. [CrossRef]
- 105. Feddersen, H.; Navarra, A.; Ward, M.N. Reduction of Model Systematic Error by Statistical Correction for Dynamical Seasonal Predictions. *J. Clim.* **1999**, *12*, 1974–1989. [CrossRef]
- 106. Kang, I.-S.; Lee, J.-Y.; Park, C.-K. Potential Predictability of Summer Mean Precipitation in a Dynamical Seasonal Prediction System with Systematic Error Correction. *J. Clim.* **2004**, *17*, 834–844. [CrossRef]
- 107. Kim, M.-K.; Kang, I.-S.; Park, C.-K.; Kim, K.-M. Superensemble prediction of regional precipitation over Korea. *Int. J. Climatol.* **2004**, 24, 777–790. [CrossRef]
- 108. Wright, C.K.; de Beurs, K.M.; Henebry, G.M. Combined analysis of land cover change and NDVI trends in the Northern Eurasian grain belt. *Front. Earth Sci.* **2012**, *6*, 177–187. [CrossRef]
- 109. Bjerke, J.W.; Rune Karlsen, S.; Arild Høgda, K.; Malnes, E.; Jepsen, J.U.; Lovibond, S.; Vikhamar-Schuler, D.; Tømmervik, H. Record-low primary productivity and high plant damage in the Nordic Arctic Region in 2012 caused by multiple weather events and pest outbreaks. *Environ. Res. Lett.* 2014, 9, 084006. [CrossRef]
- 110. Esau, I.; Miles, V.V.; Davy, R.; Miles, M.W.; Kurchatova, A. Trends in normalized difference vegetation index (NDVI) associated with urban development in northern West Siberia. *Atmos. Chem. Phys.* **2016**, *16*, 9563–9577. [CrossRef]
- 111. Gong, D.Y.; Shi, P.J. Northern hemispheric NDVI variations associated with large-scale climate indices in spring. *Int. J. Remote Sens.* **2003**, *24*, 2559–2566. [CrossRef]



© 2019 by the authors. Licensee MDPI, Basel, Switzerland. This article is an open access article distributed under the terms and conditions of the Creative Commons Attribution (CC BY) license (http://creativecommons.org/licenses/by/4.0/).